Article

Intrinsic multiferroicity in molybdenum oxytrihalides nanowires

Check for updates

Chao Yang [1], Yin Wang[2], Menghao Wu[3] ✉ & Tai Min [1,4] ✉

Low-dimensional multiferroics, which simultaneously possess at least two primary ferroic order parameters, hold great promise for post-Moore electronic devices. However, intrinsic one-dimensional (1D) multiferroics with the coexistence of ferroelectricity and ferromagnetism are still yet to be realized, which will be not only crucial for exploring the interplay between low-dimensionality and ferroelectric/ferromagnetic ordering but also significant in rendering application approaches for high density information technologies. Here, we present a theoretical prediction of intrinsic multiferroicity in 1D molybdenum oxytrihalides nanowires, especially focusing on $MoOBr_3$ nanowires which could be readily extracted from experimentally synthesized van der Waals $MoOBr_3$ bulk materials. Due to the spatial inversion symmetry spontaneously broken by Mo atoms' displacements, $MoOBr_3$ nanowires exhibit 1D ferroelectricity with small coercive electric field and exceptional Curie temperature (~570 K). Additionally, $MoOBr_3$ nanowires also possess 1D antiferroelectric metastable states. On the other hand, both ferroelectric and antiferroelectric $MoOBr_3$ nanowires exhibit ferromagnetic ordering on account of the half-filled Mo-d_{yz} orbitals, a moderate tensile strain (~5%) can greatly boost the spontaneous polarization (~40%) and a mild compress strain (~−2%) may readily switch the magnetic easy axis of ferroelectric $MoOBr_3$ nanowires. Our work holds potential candidates for developing innovative devices that exploit intrinsic multiferroic properties, enabling advancements in novel electronic and spintronic applications.

Ferroic materials are a family of materials that exhibit switchable order parameters, including electric polarization, spin polarization, or strain, in which the order parameters can be switched by external fields like electric fields, magnetic fields, or stress fields[1]. Multiferroic materials with the coexistence of electric and spin polarizations have garnered substantial attention due to the application in magnetoelectric functionality[2–5]. However, they are not abundant in nature due to the mutual exclusive origin of the two order parameters in most instances (empty d shells for electric polarization and partially filled d shells for spin polarization)[6]. In general, there are two types of multiferroics. The multiferroics whose electric polarization and spin polarization occur independently are defined as type-I, in which two kinds of ferroic orders exhibit weak coupling. In contrast, type-II multiferroics show strong coupling of their electric polarization and spin polarization[7]. The research for multiferroics had been focused on three-dimensional (3D) materials at first, leading to the discovery of various type-I and type-II multiferroics. Type-I multiferroics include the distortion induced by lone pair electrons in $BiFeO_3$[8,9] and $PbNiO_3$[10], geometric

ferroelectricity in $YMnO_3$[11,12] and $Ca_3Mn_2O_7$[13], charge ordering in $LuFe_2O_4$[14] and Fe_3O_4[15]. Type-II multiferroics, such as $TbMnO_3$[16,17] and $YBaCuFeO_5$[18], exhibit polar ordering driven by magnetic ordering.

In the past decade, significant breakthroughs have been made in the field of two-dimensional (2D) ferroics, including 2D ferroelectric (FE) materials like SnTe, MX (M = Ge, Sn, X = S, Se), In_2Se_3, $CuInP_2S_6$[19–26], and 2D ferromagnetic (FM) materials like CrI_3 and Fe_3GeTe_2[27–30]. Inspired by the progress in 2D FE and FM materials, the research on 2D multiferroics has gained attention, and several 2D multiferroics have been investigated, including $Hf_2VC_2F_2$, $CuMP_2X_6$ (M = Cr, V, X = S, Se), $ReWCl_6$, $Cr(pyz)_2$, Co_2CF_2, VOX_2 (X = Cl, Br, I)[31–38]. Recently, the study on one-dimensional (1D) ferroic materials has also emerged. Several 1D FE materials, such as GeS/SnS, WOX_4 (X = F, Cl, Br), $NbOX_3$ (X = Cl, Br, I), and VOF_3 have been theoretically studied[39–42]. Besides, the research for 1D FM materials also makes breakthrough, for example $CrSbSe_3$ and Ca_2MnO_3X (X = Cl, Br)[43,44].

However, the exploration of intrinsic multiferroicity, characterized by the coexistence of ferroelectricity and ferromagnetism in 1D materials, is

[1]Center for Spintronics and Quantum Systems, State Key Laboratory for Mechanical Behavior of Materials, School of Materials Science and Engineering, Xi'an Jiaotong University, Xi'an, 710049, China. [2]Department of Physics, International Center for Quantum and Molecular Structures, Shanghai University, Shanghai, 200444, China. [3]School of Physics, Huazhong University of Science and Technology, Wuhan, 430074, China. [4]School of Materials Science and Intelligent Engineering, Nanjing University, Suzhou, 215163, China. ✉e-mail: wmh1987@hust.edu.cn; tai.min@mail.xjtu.edu.cn

still yet to be realized. The realization of such materials is crucial for understanding the relationship between low-dimensionality and FE/FM ordering, and these studies can provide potential candidates for the development of high-density information storage devices. In this work, we predicted the existence of robust type-I multiferroicity in 1D MoOBr$_3$ nanowires whose bulk phase has been successfully synthesized in experiments. Our findings indicate that this material exhibits spontaneous polarization (P$_S$) along the wire axis, with high Curie temperature (~570 K) far above room temperature (300 K) and small coercive electric field (~0.56 MV/cm). This material, in addition, also possesses antiferroelectric (AFE) structures, which are metastable compared to FE structures. Both FE and AFE structures exhibit FM properties with calculated FM Curie temperatures for the FE and AFE structures are 9.5 and 9.3 K, respectively. We also found that tensile strain (~5%) can distinctly boost the ferroelectric polarization (~40%) and compress strain may readily switch the easy axis of FE MoOBr$_3$ nanowires. To further demonstrate the multiferroicity in molybdenum oxytrihalides family, we also performed calculations for MoOCl$_3$ and MoOI$_3$ nanowires. This study marks the first reported analysis of intrinsic type-I multiferroicity in 1D materials. Our findings propose a novel 1D system encompassing both inherent electric and spin polarizations, offering significant promise for developing new electronic and spintronic devices based on 1D multiferroics.

Results and discussion
Structural and ferroelectric properties
The chemical synthesis of 1D transition metal oxytrihalides MOX$_3$ in bulk phase, wherein M represents a transition metal and X denotes a halogen element, was initiated at an early stage, for instance MoOBr$_3$, WOX$_3$ and NbOX$_3$ (X = Cl, Br, I)[45–47]. Recently, a modified method has been successfully employed to synthesize bulk phase of van der Waals 1D MoOBr$_3$ nanowires, followed by a comprehensive investigation of its magnetic properties[48]. Sublimation method has been successfully utilized to extract a single van der Waals nanowire from bulk phase[49,50], and this method makes obtaining a purely single MoOBr$_3$ nanowire possible.

Here, we employ first-principles calculations to investigate the FE and FM properties of 1D MoOBr$_3$ nanowires. The bulk phase structure of MoOBr$_3$, presented in Fig. 1a, is characterized by a tetragonal crystal lattice

with the P4$_2$nm space group. There are two MoOBr$_3$ nanowires within a bulk unit cell (dash line square), and the calculated alignment of polarization directions in both MoOBr$_3$ nanowires suggests that the bulk structure of MoOBr$_3$ demonstrates FE behavior. This phenomenon is distinguished from bulk of 1D SnS/GeS that exhibit an AFE bulk phase[39], so it is likely that FE polarization can be detected in bulk MoOBr$_3$ without the necessity of exfoliation (See detail in Supplementary Fig. 1). In order to ascertain the potential for exfoliating MoOBr$_3$ nanowires from bulk phase, the binding energy was calculated and found to be 0.102 J/m^2, which is much smaller than the binding energies of black phosphorene (~0.358 J/m^2)[51] and MoS$_2$ (~0.422 J/m^2)[52]. For 1D MoOBr$_3$ nanowires, the axis direction, also referred to as the periodic direction, is along the 'a' direction (Fig. 1b). There exhibits two MoO$_2$Br$_4$ octahedral units in one unit cell, with two Br atoms shared between the octahedral units situated at the central position along the 'b' (long radius) direction, as depicted in Fig. 1b. In the fully relaxed structure of MoOBr$_3$ nanowires, it is observed that two Mo atoms, denoted as Mo1 and Mo2, possess displacements along the axis direction, so the structure breaks its centrosymmetry and exhibits a polar symmetry space group known as Pmm2. To quantify the displacements, we define the distortion distances d$_1$ and d$_2$, which represent the respective magnitudes of distortion of Mo1 and Mo2. In Fig. 1c, we define d$_1$ = d$_2$ > 0 (< 0) as phase A (A') that is a polar structure with polarization P$_1$ = P$_2$ > 0 (< 0). In addition, we name the structure as phase B (B') when d$_1$ = −d$_2$ > 0 (< 0), accompanied by a polarization P$_1$ = −P$_2$ > 0 (< 0), and phase B (B') is characterized by a nonpolar space group identified as P2/m. The intermediate phase between A (B) and A' (B'), denoted as the phase C, maintains centrosymmetry with d$_1$ = d$_2$ = 0 and corresponds to the space group Pmmm. By performing free-energy calculations and analyzing the parameter space of d$_1$ and d$_2$ (Fig. 1d), it is found that the Mo-displaced polar phases A and A' are indeed the ground states with degeneracy in energy, and these two phases are separated by the Mo-nondisplaced centrosymmetric phase C along the counter-diagonal direction (d$_1$ = d$_2$). More importantly, the energy curve exhibits a characteristic anharmonic double-well shape commonly observed in FE materials in the counter-diagonal direction. Besides, the Mo-displaced nonpolar phases B and B' also exhibit energy degeneracy and are separated by phase C along the main diagonal direction (d$_1$ = −d$_2$). However, it is critical to note that B and B' are metastable phases as their anharmonic

Fig. 1 | Structural configurations and energy map.
a The side view of MoOBr$_3$ bulk phase, where Mo atoms show as green balls, O atoms show as red balls and Br atoms show as brown balls. The periodic direction of MoOBr$_3$ nanowires is along 'a' direction, and the dash line shows one unit bulk cell.
b The three-dimensional (3D) view (top panel), top view (middle panel) and front view (bottom panel) of a single MoOBr$_3$ nanowire, and dash line indicates one unit cell in which two Mo atoms are named Mo1 and Mo2, respectively. **c** Top views of two energy degenerate Mo-displaced polar structures with opposite polarization (phases A and A'), two energy degenerate Mo-displaced nonpolar structures without polarization (phases B and B') and Mo-nondisplaced centrosymmetric structure (phase C). **d** The free energy contour plot of single MoOBr$_3$ nanowires as a function of displacement of Mo1 (d$_1$) and displacement of Mo2 (d$_2$). The positions of phases A', A, B, B' and C are indicated on the contour plot.
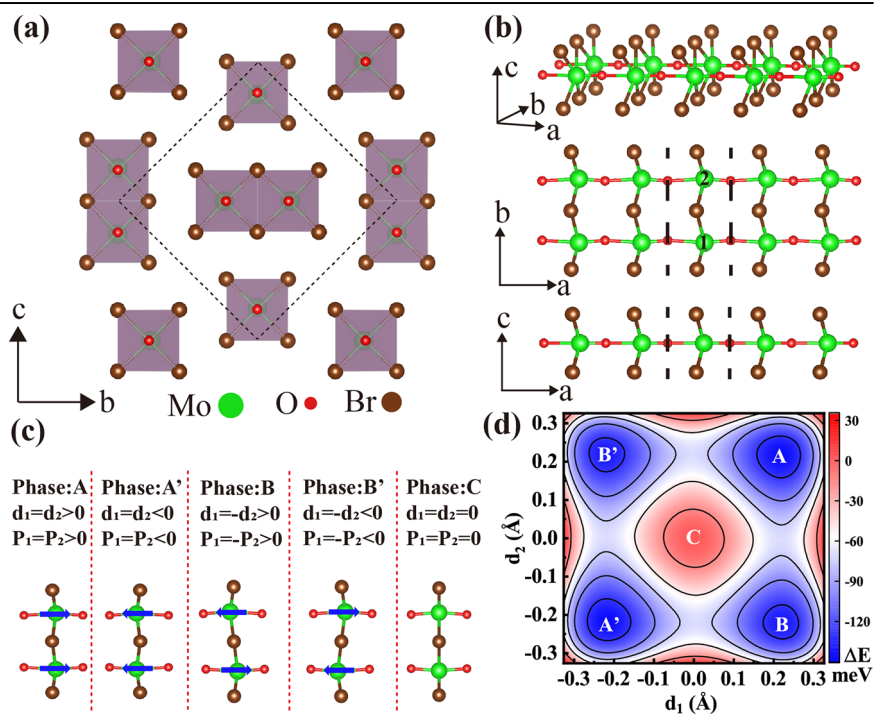
energy double-well is approximately 5 meV shallower than that of A and A', and both of B and B' do not possess polarization throughout the entire unit cell due to the equal and opposite nature of P_1 and P_2.

The presence of ferroelectricity is often associated with the existence of soft optical modes in the Brillouin zone center of the corresponding centrosymmetric structure[53–55]. To thoroughly investigate the potential polar structures in $MoOBr_3$, the Mo-nondisplaced centrosymmetric structure (phase C) is defined as paraelectric (PE) structure, in which four Mo-O bonds, four Mo-Br bonds in middle, and four Mo-Br bonds in edge are equivalent, respectively, and all O-Mo-Br bond angles are 90°. It is obvious that the positive and negative charge center are coincident in the paraelectric structure. In PE structure, Fig. 2a illustrates that there are two soft optical modes, denoted as λ_1 and λ_2, located in the Brillouin zone center, and these soft modes indicate the dynamical instability of 1D PE $MoOBr_3$ system. Further analysis of soft modes vibration reveals that λ_1 and λ_2 correspond to the displacements of two Mo atoms along axis the direction, in which the displacements can be either in the same direction (λ_1) or in opposite directions (λ_2). Remarkably, the presence of these soft modes induces spontaneous transitions towards either phase A (A') or phase B (B'), as is shown in Fig. 2b. As for phase A (A'), although four Mo-Br bonds in middle

and four Mo-Br bonds in edge are still equal respectively, four Mo-O bonds are not equal (2.153 Å for two longer Mo-O bonds and 1.687 Å for two shorter Mo-O bonds) due to the displacements of two Mo atoms, leading to the separation of positive and negative charge centers. What's more, this separations in two MoO_2Br_4 octahedral units are the same and there exhibits polarization in a whole $MoOBr_3$ unit cell, so phase A (A') is named as FE structure. With regard to phase B (B'), although Mo atoms have displacements, the polarization directions are inverse in both MoO_2Br_4 octahedral units. Therefore, the whole $MoOBr_3$ unit cell does not show FE polarization, and we define phase B (B') as AFE structure. The phonon spectra were thoroughly analyzed to ascertain the dynamical stability of FE and AFE structures, and there is no negative frequency is observed in the phonon spectra (Fig. 2a), providing further confirmation of the stability of the FE and AFE structures.

The polarization switching phenomenon plays a significant role in FE materials, as it enables desirable functionalities and applications. In this study, we designed and investigated two distinct paths for polarization switching in FE $MoOBr_3$, as illustrated in Fig. 2c. Path-I indicates the displacements of two Mo atoms reverse synchronously, passing through the PE structure (phase C), and the polarization switching occurs concomitantly

Fig. 2 | Dynamical analysis and ferroelectric properties. a Phonon spectra for FE, PE and AFE structures from left to right, in which λ_1 and λ_2 indicates two soft optical phonon modes. **b** The vibrational modes of the imaginary mode λ_1 and λ_2 in **a**. **c** Two different FE switching paths and their energy barriers. **d** Free energy as a function of polarization. Red dots are the DFT results and blue line is from model fit. **e** Ferroelectric polarization as a function of temperature (red). The differential curve of polarization with respect to temperature (blue). **f** The FE hysteresis loop simulated by Monte Carlo calculations at room temperature (300 K).
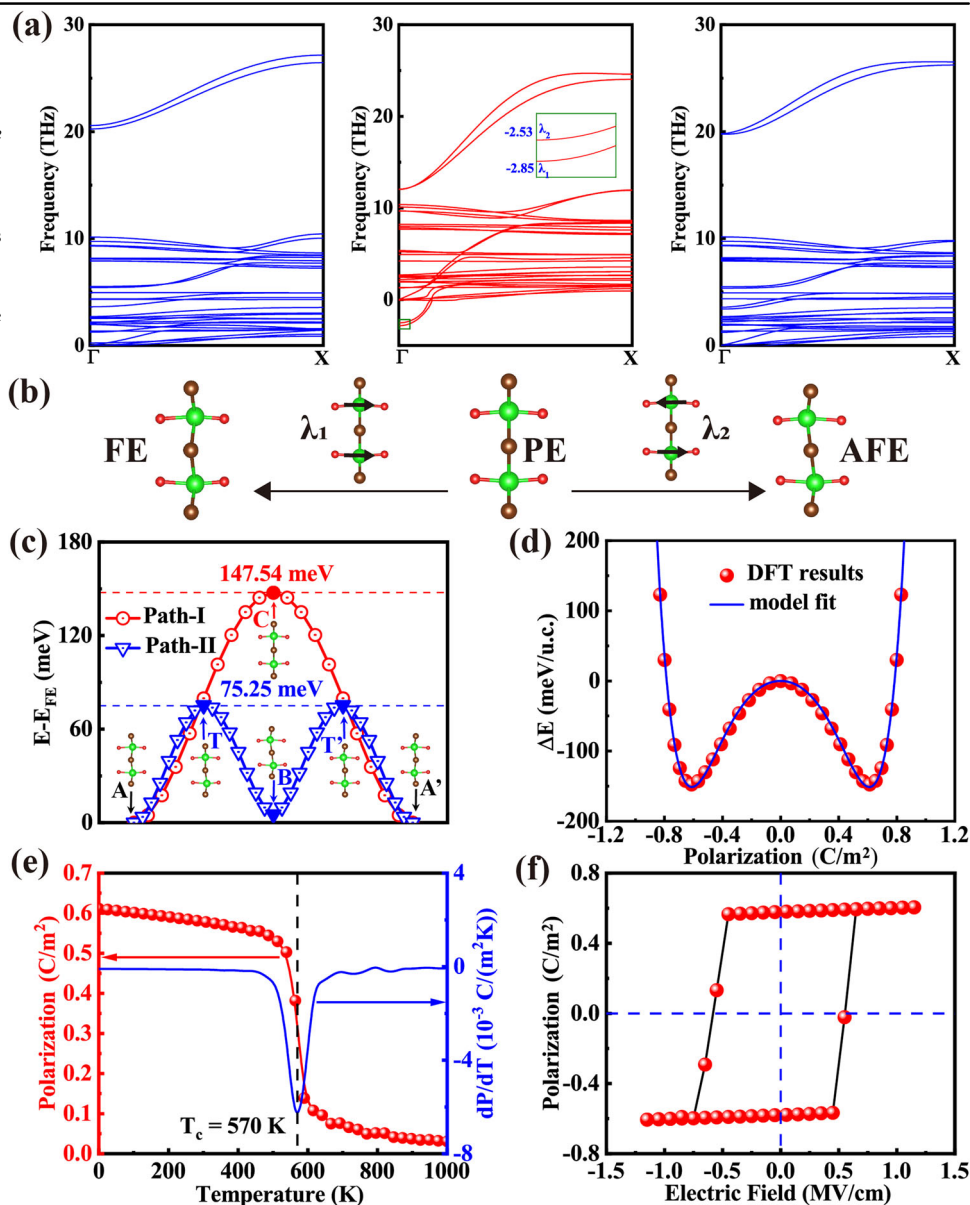
with the collective movement of the two Mo atoms. In contrast, Path-II demonstrates the displacements of two Mo atoms reverse independently. One Mo atom undergoes a reversal in displacement, while the other remains unchanged, resulting in an intermediate AFE state (phase B). Subsequently, the unchanged Mo atom also reverses its displacement, realizing the transition from phase A to A'. As is shown in Fig. 2c, the calculated energy barriers for path-I and path-II are 147.54 and 75.25 meV respectively, underscoring path-II is greater feasibility and efficiency in polarization switching compared to path-I.

To demonstrate the FE properties of MoOBr$_3$, we have calculated the FE dipole value of MoOBr$_3$ nanowires to be 3.81 eÅ per unit cell (u.c.) based on Berry phase method[56,57]. The P$_S$ value is defined as the FE dipole value divided by pure nanowire volume without the inclusion of vacuum, and the P$_S$ is aligned with the axis direction with a value of 0.61 C/m^2, which is larger than that of 2D SnTe (~0.22 C/m^2)[19] and CuInP$_2$S$_6$ (~0.15 C/m^2)[24]. For practical applications, it is crucial to ensure that the critical temperature, T$_C$, of 1D FE MoOBr$_3$ is sufficiently high to maintain polarization above room temperature. To investigate the impact of finite temperature, Monte Carlo (MC) simulations are performed, in which the Landau-Ginzburg-type expansion with the polarization serving as the order parameter[20] is adopted to explore the variation of the free energy:

$$E = \sum_i \left[\frac{A}{2}\left(P_i^2\right) + \frac{B}{4}\left(P_i^4\right) + \frac{C}{6}\left(P_i^6\right) \right] + \frac{D_a}{2} \sum_{\langle i,j \rangle_a} \left(P_i - P_j\right)^2$$
$$+ \frac{D_b}{2} \sum_{\langle i,j \rangle_b} \left(P_i - P_j\right)^2 \tag{1}$$

in which i and j represent different MoO$_2$Br$_4$ octahedral units. The first three terms describe the energy contribution from polarization in each MoO$_2$Br$_4$ octahedral unit, capturing the anharmonic double-well potential depicted in Fig. 2d. The dipole-dipole coupling in the nearest-neighbor along the 'a' and 'b' directions, represented by coefficients D$_a$ and D$_b$ respectively, is crucial for stabilizing the FE ordering. The calculation methods of D$_a$ as well as D$_b$ are shown in Supplementary Fig. 3, and the values of coefficients A, B, C, D$_a$ and D$_b$ are summarized in Supplementary Table 2. Figure 2e illustrates the average polarization values as a function of temperature (red dots), in which blue line exhibits a sharp drop of polarization at a temperature near T$_C$ (~570 K), indicating the occurrence of a phase transition[39]. More significantly, the predicted T$_C$ is much higher than the experiment reported T$_C$ of 2D FE SnTe (~270 K)[19] and CuInP$_2$S$_6$ (~320 K)[24]. To verify the thermal stability of FE and AFE MoOBr$_3$ structures, ab initio molecular dynamics (AIMD) simulations are employed, and the results

(Supplementary Fig. 4) confirm the thermal stability of both structures at room temperature (300 K). Figure 2f shows the MC simulated hysteresis loop of FE MoOBr$_3$ nanowires at room temperature, and the coercive electric field is around 0.56 MV/cm. Compared to the coercive electric field of 2D FE In$_2$Se$_3$ (~10 MV/cm)[23] and CuInP$_2$S$_6$ (~10 MV/cm)[24], the small coercive electric field of MoOBr$_3$ nanowires indicates its great potential for low power FE devices. The structural and FE parameters of both FE and AFE structures are summarized in Table 1 as below.
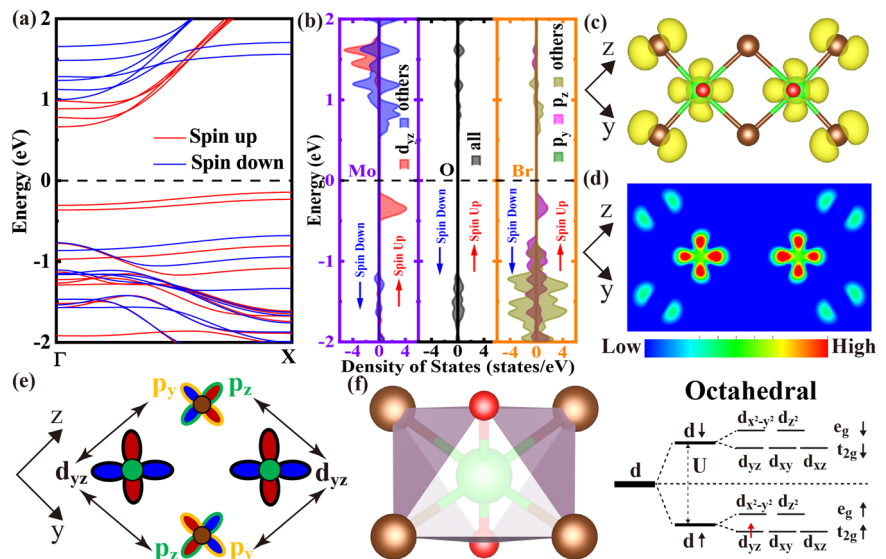
Electronic and ferromagnetic properties
In addition to the studies of FE properties, we also investigated the electronic band structures of MoOBr$_3$ nanowires. The valence states of Mo, O, and Br are +5, −2, and −1 respectively, so magnetism may appear because Mo-4d orbitals have an unbonded electron. Figure 3a displays the band structure of FE MoOBr$_3$ with a FM ground state, which will be further discussed in subsequent sections. It is noteworthy that FE MoOBr$_3$ behaves as a semiconductor with an indirect band gap of approximately 0.81 eV. All three structures (FE, AFE, and PE structures) exhibit FM spin polarization, with a total magnetic moment of 1 μ$_B$ per MoO$_2$Br$_4$ octahedral unit. The partial density of states (PDOS) depicted in Fig. 3b reveals the DOS of the band structure in Fig. 3a, and PDOS results of AFE and PE MoOBr$_3$ refer to the Supplementary Figure 5. To gain further insights, a real-space charge distribution analysis of the top two valence bands is conducted (Fig. 3c), along with a cross-section analysis of the partial charge distribution (Fig. 3d). These investigations indicate that the magnetic moment predominantly arises from the Mo-d_{yz} orbitals. The coupling between the Mo-d_{yz} and O-p orbitals is negligible within the Slater-Koster approximation[58], therefore, the movement of Mo along the axis direction is not hindered by the Mo-d_{yz} orbitals. Considering the configuration of Mo−Br−Mo, which approximates a right angle, and applying the Goodenough-Kanamori-Anderson rules[59–61], it is inferred that a superexchange occurs in the Mo-Br-Mo bond

Table 1 | Calculated lattice parameter a (Å), Mo displacement d (Å), and spontaneous polarization P_S (C/m^2) in one unit cell of 1D FE and AFE MoOBr$_3$ nanowires, FE Curie temperature TC (K) of and coercive electric field EC (MV/cm) at room temperature (300 K) of 1D FE MoOBr$_3$ nanowires

	a	d	P_S	T_C	E_C
FE	3.84	0.233	0.61	570	0.56
AFE	3.84	0.246	0	/	/

Fig. 3 | Electronic results for ferroelectric MoOBr$_3$ nanowires. a, b The band structure and partial density of states. **c, d** The partial charge distribution with isosurface equals to 0.004 e/Bohr^3 and the cross section for partial charge of top two valance bands. **e** The nearly 90°superexchange diagram for Br-Mo-Br which describes the short-range magnetic ordering along the 'b' direction. **f** Left: The 3D view of MoO$_2$Br$_4$ octahedral unit. Right: The corresponding Mo-d orbitals splitting and occupation for MoO$_2$Br$_4$ octahedral unit.

Fig. 4 | Ferromagnetic properties. a The considered four magnetic configurations, including ferromagnetic state and three antiferromagnetic (AFM) states. Yellow and blue isosurfaces of 0.02 e/Bohr^3 are corresponding to positive and negative spin density, respectively. **b** The average value of magnetization changes with temperature for FE MoOBr$_3$ (red). The differential curve of magnetization with respect to temperature (blue). **c** The energies difference among three AFM states and FM state in **a** change with MoOBr$_3$ from PE (normalized value is 0) structure to FE structure (normalized value is 1), in which the energy value of FM is set as reference value of zero. **d** The magnetic anisotropy energies (MAE) per Mo atom change with MoOBr$_3$ from PE structure (normalized value is 0) structure to FE structure (normalized value is 1).
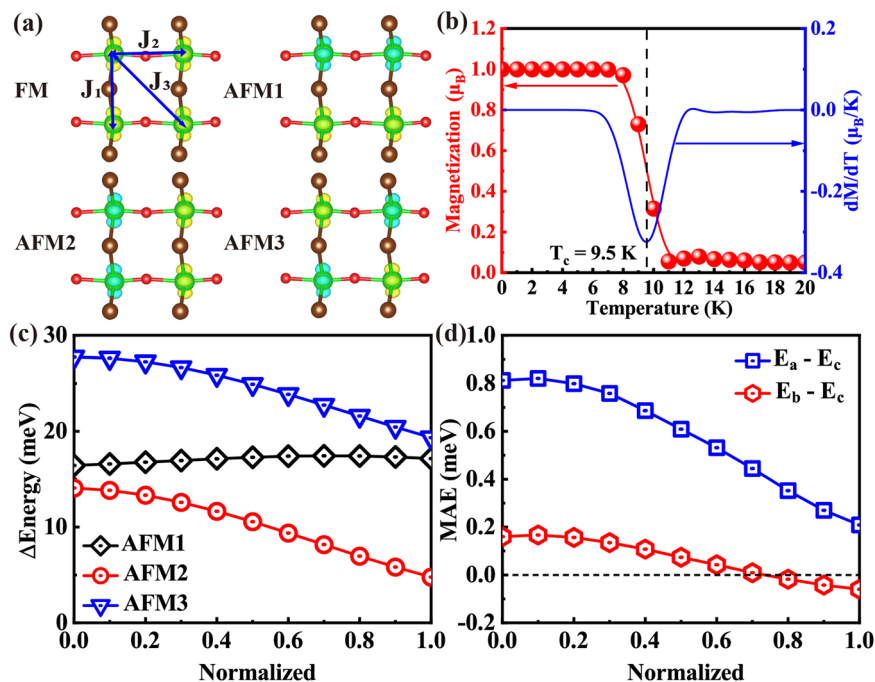
via the p_y or p_z orbitals of Br, favoring FM ordering (Fig. 3e). In accordance with the crystal field effects observed in octahedral complexes, the d_{z^2} and $d_{x^2-y^2}$ orbitals (e_g orbitals) lie directly in the path of the approaching ligands[62]. Electrons in these orbitals experience a greater force of repulsion compared to those in the d_{yz}, d_{xy}, and d_{xz} orbitals (t_{2g} orbitals) that are directed in the space between the approaching ligands. Consequently, the energy of the e_g orbitals increases due to the greater repulsion, while that of the t_{2g} orbitals decreases. The splitting of the Mo-d orbitals is illustrated in Fig. 3f, and it can be deduced that the d_{yz} orbital exhibits a spin-up electron occupation, consistent with the previous partial charge analysis.

Like FE phase transition, the Curie temperature for FM phase transition is also a crucial parameter. To determine the energetically preferred magnetic ordering in MoOBr$_3$, we employed a double cells configuration along the axis direction, where FM configuration and three antiferromagnetic (AFM) configurations were considered to explore the long-range magnetic ordering in FE MoOBr$_3$, as illustrated in Fig. 4a. The presence of magnetic anisotropy is essential for stabilizing long-range magnetic ordering in 2D and 1D materials, as it overcomes the Mermin-Wagner restriction[63], so we took the spin-orbit coupling (SOC) into account to evaluate the magnetic anisotropy energy (MAE) of MoOBr$_3$. The magnetization direction was set along the 'a', 'b', and 'c' (short radius) directions respectively, among them that the most stable state corresponds to the 'b' direction while the highest energy state aligns along the 'a' direction. In order to effectively describe the FM interactions in MoOBr$_3$, we constructed the following spin Hamiltonian:

$$\widehat{H} = -\sum_{\langle ij \rangle} J_1 \vec{S}_i \cdot \vec{S}_j - \sum_{\langle kl \rangle} J_2 \vec{S}_k \cdot \vec{S}_l - \sum_{\langle mn \rangle} J_3 \vec{S}_m \cdot \vec{S}_n + K \sum_{\langle i \rangle} (\vec{S}_i^z)^2 \quad (2)$$

in which the summation $\langle ij \rangle$ and $\langle kl \rangle$ include all the nearest-neighbor exchange interactions along 'b' and 'a' direction respectively, and the summation $\langle mn \rangle$ includes the next-nearest-neighbor exchange interactions. Last term denotes the magnetic anisotropy, which is defined as the energy difference per Mo atom of the hard axis and easy axis. The parameters J_1, J_2, J_3, and K were extracted from the first-principles calculations, yielding values 3.964, 0.412, 0.161, and 0.269 meV, respectively (more details are given in Supplementary Information). The FM transition temperature was estimated using the MC simulations based on this spin model, and the obtained FM transition temperature for FE MoOBr$_3$ is

around 9.5 K[64]. For AFE MoOBr$_3$, the corresponding FM transition temperature is approximately 9.3 K (Supplementary Fig. 6).

Moreover, we made a tentative evaluation of the magnetoelectric coupling by monitoring the magnetism response to variations in FE polarization, achieved by transitioning Mo atoms from PE state to FE state. Figure 4c illustrates the corresponding energy dependence of the four magnetic configurations relative to FE structures, in which the ground state consistently maintains the FM ordering for FE MoOBr$_3$ while the lowest energy AFM state exhibits AFM2 ordering. As MoOBr$_3$ transitions from PE to FE structure, the energy difference between AFM2 state and FM state decreases, and the FM easy axis shifts from 'c' direction to 'b' direction. Additionally, the MAE for magnetization along the 'a' direction is always the highest, as depicted in Fig. 4d. The relative results of MoOBr$_3$ transitioning from PE to AFE structure exhibit similarities to the consequences observed during the transition from PE to FE structure (details can be found in Supplementary Fig. 6). The FM parameters of both FE and AFE structures are concluded in Table 2 as below.

Regulation of multiferroicity by strain

Strain is a highly effective method for regulating FE polarization and exerting influence on magnetic properties of materials, and the axis strain is applied to FE MoOBr$_3$ to investigate the change of FE and FM properties, as illustrated in Fig. 5a. The comprehensive results clearly demonstrate positive correlations between both the displacements of Mo atoms and the polarization value with strain, and a 40% increase in the polarization value is observed when strain reaches 5% (Fig. 5b). To illustrate the significance of this finding, we compared our results to 2D systems with comparable FE switch barrier and

Table 2 | Calculated band gap E_g (eV), magnetic exchange coupling parameters J_1, J_2, and J_3 (meV), magnetic anisotropy energy K (meV), FM Curie temperature $T_{C\text{-}FM}$ (K) of 1D FE and AFE MoOBr$_3$ nanowires

	E_g	J_1	J_2	J_3	K	$T_{C\text{-}FM}$
FE	0.81	3.964	0.412	0.161	0.269	9.5
AFE	0.79	4.012	0.475	0.078	0.363	9.3

Fig. 5 | Regulation of multiferroicity by strain.
a Strain direction for FE MoOBr$_3$ nanowires.
b Alteration of Mo's displacement with regard to strain (red). Variation of polarization changes with strain (blue). **c** The energy difference among three AFM states and FM state as functions of strain.
d Change of the MAE per Mo atom with regard to strain, in which red dots indicate MAE between 'c' and 'b' directions and blue dots represent MAE between 'a' and 'b' directions.
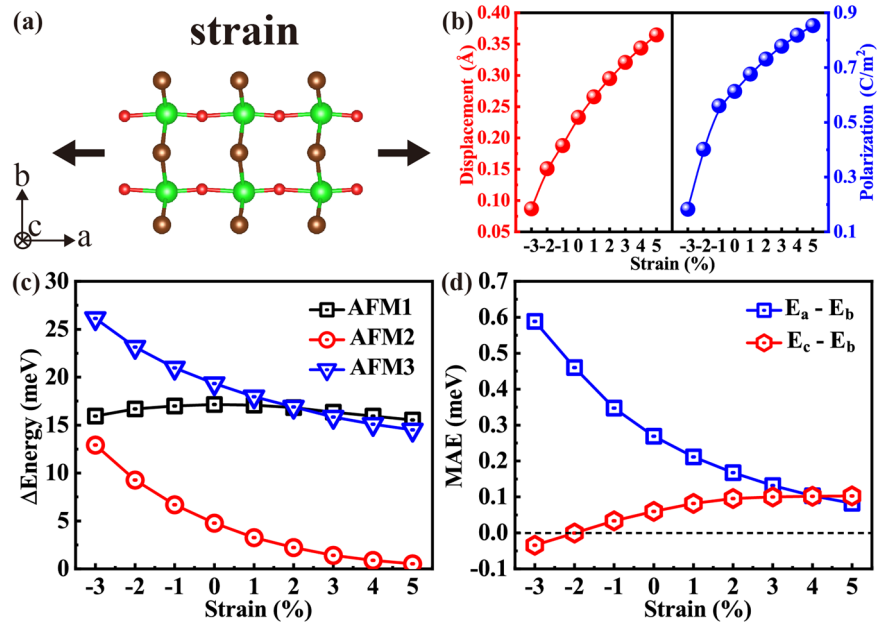
FE dipole value, using the well-studied 2D α-GeSe as an example (barrier: ~137 meV, dipole: ~3.95 eÅ/u.c.). In the case of α-GeSe, an increase of approximately 10% in polarization value is observed under a uniaxial 5% strain applied along the polarization direction[21], highlighting the giant response of polarization to strain in our FE MoOBr$_3$ nanowires. With regards to the magnetic properties, the material maintains FM state when the strain varies from −3% to 5%. However, a notable finding emerges when the strain exceeds 2%, the energy of AFM3 state becomes lower than that of AFM1, despite AFM2 exhibiting the lowest energy among the three AFM states (Fig. 5c). Throughout the range of strains from −3% to 5%, a remarkable switch of the easy axis from 'c' direction to 'b' direction is observed when the strain is around −2%, and 'c' direction even become the hardest axis if the strain larger than 4%, as depicted in Fig. 5d.

Finally, we can confirm the type of multiferroicity exhibited in 1D MoOBr$_3$ nanowires by discussing the origin and coupling of ferroelectricity and ferromagnetism. Based on the previous results, it is evident that ferroelectricity of MoOBr$_3$, which combines contributions of ionic polarization and electronic polarization, arises from the displacements of Mo atoms. In this case, it is noteworthy that the absolute value of ionic polarization (0.95 C/m^2) is approximately three times larger than that of electronic polarization (0.34 C/m^2), despite their opposite directions (refer to the Supplementary Figure 2 for more details). On the other hand, ferromagnetism in MoOBr$_3$ can be attributed to the presence of half-filled Mo-d_{yz} orbitals, as indicated by electronic analysis. Importantly, MoOBr$_3$ system consistently maintains a FM state as it transitions from PE structure to FE/AFE structure, though the magnetic easy axis changes from PE to FE structure. Therefore, we can conclude that there is an intrinsic type-I multiferroicity presenting in 1D MoOBr$_3$ nanowires, in which the electric polarization and spin polarization show weak coupling. What's more, the Dzyaloshinskii-Moriya interaction may exist in FE MoOBr$_3$ nanowires (Supplementary Fig. 8), based on the investigation on 2D type-I multiferroic VOI$_2$[65,66]. To further broaden the multiferroicity in MoOX$_3$ (X = Cl, Br, I) family, we also performed calculations for MoOCl$_3$ and MoOI$_3$ nanowires (see results in Supplementary Information).

In summary, our study has presented the prediction of intrinsic type-I multiferroicity in one-dimensional MoOBr$_3$ nanowires. The nanowires exhibit both ferroelectric and antiferroelectric structures, the polarization arises from the displacements of Mo atoms, and the ferroelectric MoOBr$_3$ nanowires possess above room temperature ferroelectric T$_C$ and small coercive electric field. Additionally, we have also discovered the presence of

ferromagnetic ordering along the radius direction in both ferroelectric and antiferroelectric MoOBr$_3$ nanowires due to the half-filled Mo-d_{yz} orbitals, leading to the inherent coexistence of ferroelectricity and ferromagnetism in one-dimensional materials. Further investigation indicated that strain can evidently boost ferroelectric polarization and readily switch ferromagnetic easy axis of ferroelectric MoOBr$_3$ nanowires. Our findings not only realize intrinsic one-dimensional multiferroicity, but also provide a practical platform for the development of nanoscale devices.

Methods
First-principles calculations details
Our first-principles calculations are performed within the density functional theory (DFT) formalism, and the calculation software package is the Vienna Ab-initio Simulation Package (VASP)[67]. The projector augmented wave (PAW)[68] method is employed to model the ionic potentials, treating the Mo 4p 5s 4d, O 2s 2p, and Br 4s 4p as valence electrons. The exchange and correlation energy are treated with the Perdew–Burke–Ernzerhof (PBE)[69] realization of the generalized gradient approximation (GGA) and the GGA + U[70] method is applied for the 4d orbitals of Mo atoms with U$_{eff}$ = 2 eV. The Heyd-Scuseria-Ernzerhof (HSE06)[71,72] functional is also adopted to compare with the GGA + U results. The energy cut-off is set to 500 eV, and a vacuum region larger than 15 Å is introduced to avoid interactions between neighboring nanowires. The van der Waals (vdW) correction is considered by DFT-D3 approach[73]. All the atoms are allowed to relax until the calculated forces were converged to 0.01 eV Å^{-1}, and the energy precision was set to be 10^{-5} eV. The energy precision was set to be 10^{-7} eV for MAE calculations. The k-point grid of 13 × 1 × 1 in the Monkhorst-Pack scheme[74] is used to sample the Brillouin zone for relaxation and self-consistent calculations. The spin−orbit coupling (SOC)[75] effect is taken into consideration for MAE calculations. The Nudged Elastic Band (NEB) method[76] is used to study the ferroelectric phase transition. Lattice dynamics calculations are performed with the Phonopy package[77], which uses the supercell finite-displacement method to obtain sets of second-order force constant matrices. The force constant matrices are calculated using 4 × 1 × 1 supercells for the FE, AFE and PE phase.

Monte Carlo simulations details
MC simulations are performed for a periodic 1D supercell containing 10^3 unit cells. The 4 × 10^5 MC steps are used for equilibration, and every simulation is repeated 3 × 10^5 times.

Molecular dynamics simulations details

Ab initio molecular dynamics (AIMD) simulations are studied by taking NVT ensemble with Nosé thermostat[78] at finite temperature by VASP code[67]. Calculations are performed on $8 \times 1 \times 1$ supercells, for a total of 6000 fs with a 1.5 fs time resolution.

Data availability

The data that support the findings of this study are available from the corresponding author upon reasonable request.

Code availability

The codes that support the findings of this study are available from the corresponding author upon reasonable request.

References

1. Man, P., Huang, L., Zhao, J. & Ly, T. H. Ferroic phases in two-dimensional materials. *Chem. Rev.* **123**, 10990–11046 (2023).
2. Balke, N. et al. Deterministic control of ferroelastic switching in multiferroic materials. *Nat. Nanotechnol.* **4**, 868–875 (2009).
3. Cheong, S. W. & Mostovoy, M. Multiferroics: a magnetic twist for ferroelectricity. *Nat. Mater.* **6**, 13–20 (2007).
4. Scott, J. F. Data storage—multiferroic memories. *Nat. Mater.* **6**, 256–257 (2007).
5. Spaldin, N. A. & Ramesh, R. Advances in magnetoelectric multiferroics. *Nat. Mater.* **18**, 203–212 (2019).
6. Hill, N. A. Why are there so few magnetic ferroelectrics? *J. Phys. Chem. B* **104**, 6694–6709 (2000).
7. Fiebig, M., Lottermoser, T., Meier, D. & Trassin, M. The evolution of multiferroics. *Nat. Rev. Mater.* **1**, 1–14 (2016).
8. Heron, J. T. et al. Deterministic switching of ferromagnetism at room temperature using an electric field. *Nature* **516**, 370–373 (2014).
9. Seidel, J. et al. Conduction at domain walls in oxide multiferroics. *Nat. Mater.* **8**, 229–234 (2009).
10. Inaguma, Y. et al. Synthesis, structural transformation, thermal stability, valence state, and magnetic and electronic properties of $PbNiO_3$ with perovskite-and $LiNbO_3$-type structures. *J. Am. Chem. Soc.* **133**, 16920–16929 (2011).
11. Van Aken, B. B., Palstra, T. T., Filippetti, A. & Spaldin, N. A. The origin of ferroelectricity in magnetoelectric $YMnO_3$. *Nat. Mater.* **3**, 164–170 (2004).
12. Lee, S. et al. Giant magneto-elastic coupling in multiferroic hexagonal manganites. *Nature* **451**, 805–808 (2008).
13. Benedek, N. A. & Fennie, C. J. Hybrid improper ferroelectricity: a mechanism for controllable polarization-magnetization coupling. *Phys. Rev. Lett.* **106**, 107204 (2011).
14. Ikeda, N. et al. Ferroelectricity from iron valence ordering in the charge-frustrated system $LuFe_2O_4$. *Nature* **436**, 1136–1138 (2005).
15. Senn, M. S., Wright, J. P. & Attfield, J. P. Charge order and three-site distortions in the Verwey structure of magnetite. *Nature* **481**, 173–176 (2012).
16. Kimura, T. et al. Magnetic control of ferroelectric polarization. *Nature* **426**, 55–58 (2003).
17. Matsubara, M. et al. Magnetoelectric domain control in multiferroic $TbMnO_3$. *Science* **348**, 1112–1115 (2015).
18. Scaramucci, A. et al. Multiferroic magnetic spirals induced by random magnetic exchanges. *Phys. Rev. X* **8**, 011005 (2018).
19. Chang, K. et al. Discovery of robust in-plane ferroelectricity in atomic-thick SnTe. *Science* **353**, 274–278 (2016).
20. Fei, R., Kang, W. & Yang, L. Ferroelectricity and phase transitions in monolayer group-IV monochalcogenides. *Phys. Rev. Lett.* **117**, 097601 (2016).
21. Priydarshi, A., Chauhan, Y. S., Bhowmick, S. & Agarwal, A. Strain-tunable in-plane ferroelectricity and lateral tunnel junction in monolayer group-IV monochalcogenides. *J. Appl. Phys.* **131**, 034101 (2022).
22. Ding, W. et al. Prediction of intrinsic two-dimensional ferroelectrics in In_2Se_3 and other III_2-VI_3 van der Waals materials. *Nat. Commun.* **8**, 14956 (2017).
23. Cui, C. et al. Intercorrelated in-plane and out-of-plane ferroelectricity in ultrathin two-dimensional layered semiconductor In_2Se_3. *Nano Lett.* **18**, 1253–1258 (2018).
24. Liu, F. et al. Room-temperature ferroelectricity in $CuInP_2S_6$ ultrathin flakes. *Nat. Commun.* **7**, 1–6 (2016).
25. Pan, X., Li, Y., Cheng, B., Liang, S. J. & Miao, F. 2D materials for intelligent devices. *Sci. China. Phys. Mech. Astron.* **66**, 117504 (2023).
26. Tan, Y. et al. Research progress on 2D ferroelectric and ferrovalley materials and their neuromorphic application. *11Sci. China. Phys. Mech. Astron.* **66**, 117505 (2023).
27. Huang, B. et al. Layer-dependent ferromagnetism in a van der Waals crystal down to the monolayer limit. *Nature* **546**, 270–273 (2017).
28. Huang, B. et al. Electrical control of 2D magnetism in bilayer CrI_3. *Nat. Nanotechnol.* **13**, 544–548 (2018).
29. Deng, Y. et al. Gate-tunable room-temperature ferromagnetism in two-dimensional Fe_3GeTe_2. *Nature* **563**, 94–99 (2018).
30. Fei, Z. et al. Two-dimensional itinerant ferromagnetism in atomically thin Fe_3GeTe_2. *Nat. Mater.* **17**, 778–782 (2018).
31. Zhang, J. J. et al. Type-II multiferroic $Hf_2VC_2F_2$ MXene monolayer with high transition temperature. *J. Am. Chem. Soc.* **140**, 9768–9773 (2018).
32. Qi, J., Wang, H., Chen, X. & Qian, X. Two-dimensional multiferroic semiconductors with coexisting ferroelectricity and ferromagnetism. *Appl. Phys. Lett.* **113**, 043102 (2018).
33. Zhang, D., Li, A., Chen, X., Zhou, W. & Ouyang, F. Tuning valley splitting and magnetic anisotropy of multiferroic $CuMP_2X_6$ (M = Cr, V, X = S, Se) monolayer. *Phys. Rev. B* **105**, 085408 (2022).
34. Wang, X. et al. Electrical and magnetic anisotropies in van der Waals multiferroic $CuCrP_2S_6$. *Nat. Commun.* **14**, 840 (2023).
35. Xu, M. et al. Electrical control of magnetic phase transition in a type-I multiferroic double-metal trihalide monolayer. *Phys. Rev. Lett.* **124**, 067602 (2020).
36. Yang, Y. et al. Two-dimensional organic–inorganic room-temperature multiferroics. *J. Am. Chem. Soc.* **144**, 14907–14914 (2022).
37. Huang, C. et al. Toward room-temperature electrical control of magnetic order in multiferroic van der Waals materials. *Nano Lett.* **22**, 5191–5197 (2022).
38. Tan, H. et al. Two-dimensional ferromagnetic-ferroelectric multiferroics in violation of the d^0 rule. *Phys. Rev. B* **99**, 195434 (2019).
39. Zhang, J. J., Guan, J., Dong, S. & Yakobson, B. I. Room-temperature ferroelectricity in group-IV metal chalcogenide nanowires. *J. Am. Chem. Soc.* **141**, 15040–15045 (2019).
40. Lin, L. F., Zhang, Y., Moreo, A., Dagotto, E. & Dong, S. Quasi-one-dimensional ferroelectricity and piezoelectricity in WOX_4 halogens. *Phys. Rev. Mater.* **3**, 111401 (2019).
41. Zhang, L., Tang, C., Sanvito, S. & Du, A. Purely one-dimensional ferroelectricity and antiferroelectricity from van der Waals niobium oxide trihalides. *npj Comput. Mater.* **7**, 135 (2021).
42. Xu, T., Zhang, J., Shimada, T., Wang, J. & Yang, H. Intrinsic atomic-scale antiferroelectric VOF_3 nanowire with ultrahigh-energy storage properties. *Nano Lett.* **23**, 9080–9086 (2023).
43. Qu, Y., Arguilla, M. Q., Zhang, Q., He, X. & Dincă, M. Ultrathin, high-aspect ratio, and free-standing magnetic nanowires by exfoliation of ferromagnetic quasi-one-dimensional van der Waals lattices. *J. Am. Chem. Soc.* **143**, 19551–19558 (2021).
44. Romero, F. D., Lepoittevin, C., Kodjikian, S., Colin, C. & Hayward, M. Ca_2MnO_3X (X = Cl, Br) oxyhalides with 1-dimensional ferromagnetic chains of square-planar S = 2 Mn^{3+}. *J. Am. Chem. Soc.* **145**, 23346–23351 (2023).

Article

45. Crouch, P. C., Fowles, G. W. A., Frost, J. L., Marshall, P. R. & Walton, R. A. Tungsten (V) oxytrichloride and oxytribromide. Part I. Preparation, structure, and a comparison with the analogous molybdenum (V) oxytrihalides. *J. Chem. Soc. A*, 1061–1064 (1968).

46. Lunk, H. J. & Hartl, H. Discovery, properties and applications of tungsten and its inorganic compounds. *ChemTexts* **5**, 15 (2019).

47. Hartwig, S. & Hillebrecht, H. Crystal structures of $NbOI_3$ and $NbOBr_3$–polar double chains in different non-centrosymmetric structures. *Z. Anorg. Allg. Chem.* **634**, 115–120 (2008).

48. Vorobyova, A. A. et al. Peculiar crystal structure and long-range order of spin-1/2 ladders in $MoOBr_3$. *J. Alloy. Compd.* **968**, 172072 (2023).

49. Xue, D. J. et al. GeSe thin-film solar cells fabricated by self-regulated rapid thermal sublimation. *J. Am. Chem. Soc.* **139**, 958–965 (2017).

50. Slade, C. A., Sanchez, A. M. & Sloan, J. Unprecedented new crystalline forms of SnSe in narrow to medium diameter carbon nanotubes. *Nano Lett.* **19**, 2979–2984 (2019).

51. Shulenburger, L., Baczewski, A. D., Zhu, Z., Guan, J. & Tomanek, D. The nature of the interlayer interaction in bulk and few-layer phosphorus. *Nano Lett.* **15**, 8170–8175 (2015).

52. Zhuang, H. L. & Hennig, R. G. Computational search for single-layer transition-metal dichalcogenide photocatalysts. *J. Phys. Chem. C.* **117**, 20440–20445 (2013).

53. Cochran, W. Crystal stability and the theory of ferroelectricity. *Adv. Phys.* **9**, 387–423 (1960).

54. Cochran, W. Crystal stability and the theory of ferroelectricity part II. Piezoelectric crystals. *Adv. Phys.* **10**, 401–420 (1961).

55. Cochran, W. Lattice vibrations. *Rep. Prog. Phys.* **26**, 1–45 (1963).

56. King-Smith, R. D. & Vanderbilt, D. Theory of polarization of crystalline solids. *Phys. Rev. B Condens. Matter Mater. Phys.* **47**, 1651–1654 (1993).

57. Resta, R. Macroscopic polarization in crystalline dielectrics: the geometric phase approach. *Rev. Mod. Phys.* **66**, 899–915 (1994).

58. Slater, J. C. & Koster, G. F. Simplified LCAO method for the periodic potential problem. *Phys. Rev.* **94**, 1498 (1954).

59. Goodenough, J. B. Theory of the role of covalence in the perovskite-type manganites [La, M(II)]MnO_3. *Phys. Rev.* **100**, 564–573 (1955).

60. Goodenough, J. B. An interpretation of the magnetic properties of the perovskite-type mixed crystals $La_{1-x}Sr_xCoO_{3-\lambda}$. *J. Phys. Chem. Solids* **6**, 287–297 (1958).

61. Kanamori, J. Superexchange interaction and symmetry properties of electron orbitals. *J. Phys. Chem. Solids* **10**, 87–98 (1959).

62. Huang, C. et al. Ultra-high-temperature ferromagnetism in intrinsic tetrahedral semiconductors. *J. Am. Chem. Soc.* **141**, 12413–12418 (2019).

63. Mermin, N. D. & Wagner, H. Absence of ferromagnetism or antiferromagnetism in one- or two-dimensional isotropic Heisenberg models. *Phys. Rev. Lett.* **17**, 1133 (1966).

64. Zhang, H., Wang, Y., Wang, H., Huo, D. & Tan, W. Room-temperature magnetoresistive and magnetocaloric effect in $La_{1-x}Ba_xMnO_3$ compounds: Role of Griffiths phase with ferromagnetic metal cluster above Curie temperature. *J. Appl. Phys.* **131**, 043901 (2022).

65. Xu, C. et al. Electric-field switching of magnetic topological charge in type-I multiferroics. *Phys. Rev. Lett.* **125**, 037203 (2020).

66. Ding, N., Chen, J., Dong, S. & Stroppa, A. Ferroelectricity and ferromagnetism in a VOI_2 monolayer: Role of the Dzyaloshinskii-Moriya interaction. *Phys. Rev. B* **102**, 165129 (2020).

67. Kresse, G. & Furthmuller, J. Efficient iterative schemes for ab initio total-energy calculations using a plane-wave basis set. *Phys. Rev. B* **54**, 11169–11186 (1996).

68. Blöchl, P. E. Projector augmented-wave method. *Phys. Rev. B* **50**, 17953–17979 (1994).

69. Perdew, J. P., Burke, K. & Ernzerhof, M. Generalized gradient approximation made simple. *Phys. Rev. Lett.* **77**, 3865–3868 (1996).

70. Anisimov, V. I., Aryasetiawan, F. & Lichtenstein, A. I. First-principles calculations of the electronic structure and spectra of strongly correlated systems: the LDA+U method. *J. Phys. Condens. Matter* **9**, 767–808 (1997).

71. Heyd, J., Scuseria, G. E. & Ernzerhof, M. Hybrid functionals based on a screened coulomb. *Potential. J. Chem. Phys.* **118**, 8207–8215 (2003).

72. Heyd, J., Scuseria, G. E. & Ernzerhof, M. Erratum: "hybrid functionals based on a screened coulomb potential". *J. Chem. Phys.* **124**, 219906 (2006).

73. Grimme, S., Ehrlich, S. & Goerigk, L. Effect of the damping function in dispersion corrected density functional theory. *J. Comput. Chem.* **32**, 1456–1465 (2011).

74. Monkhorst, H. J. & Pack, J. D. Special points for brillouin-zone integrations. *Phys. Rev. B* **13**, 5188–5192 (1976).

75. Koelling, D. D. & Harmon, B. N. A technique for relativistic spin-polarized calculations. *J. Phys. C Solid State Phys.* **10**, 3107–3114 (1977).

76. Henkelman, G., Uberuaga, B. P. & Jonsson, H. A climbing image nudged elastic band method for finding saddle points and minimum energy paths. *J. Chem. Phys.* **113**, 9901–9904 (2000).

77. Togo, A. & Tanaka, I. First principles phonon calculations in materials science. *Scr. Mater.* **108**, 1–5 (2015).

78. Nosé, S. A unified formulation of the constant temperature molecular dynamics methods. *J. Chem. Phys.* **81**, 511–519 (1984).

Acknowledgements

Author contributions
C.Y. performed the calculation, analysis of the result, and draft writing. Y.W. provided computing resources. M.W. and T.M. discussed the results, provided many suggestions and performed the supervision and writing-review.

Competing interests
The authors declare no competing interests.

Additional information
Supplementary information The online version contains supplementary material available at https://doi.org/10.1038/s41524-024-01368-6.

Correspondence and requests for materials should be addressed to Menghao Wu or Tai Min.

Reprints and permissions information is available at http://www.nature.com/reprints

Publisher's note Springer Nature remains neutral with regard to jurisdictional claims in published maps and institutional affiliations.